Comparisons and quality control of wind observations in a mountainous city using wind profile radar and the Aeolus satellite

Hua Lu[1, 3], Min Xie[1,2], Wei Zhao[4], Bojun Liu[5], Tijian Wang[1], Bingliang Zhuang[1]

[1]School of Atmospheric Sciences, Nanjing University, Nanjing 210023, China
[2]School of Environment, Nanjing Normal University, Nanjing 210023, China
[3] Chongqing Institute of Meteorological Sciences, Chongqing 401147, China
[4]Nanjing Institute of Environmental Sciences, Ministry of Ecology and Environment of the People's Republic of China, Nanjing 210023, China
[5]Chongqing Meteorological Observatory, Chongqing 401147, China

Comparisons and quality control of wind observations in a mountainous city using wind profile radar and the Aeolus satellite

Hua Lu[1, 3], Min Xie[1,2], Wei Zhao[4], Bojun Liu[5], Tijian Wang[1], Bingliang Zhuang[1]

[1]School of Atmospheric Sciences, Nanjing University, Nanjing 210023, China

[2]School of Environment, Nanjing Normal University, Nanjing 210023, China

[3] Chongqing Institute of Meteorological Sciences, Chongqing 401147, China

[4] Nanjing Institute of Environmental Sciences, Ministry of Ecology and Environment of the People's Republic of China,Nanjing 210023, China

[5]Chongqing Meteorological Observatory, Chongqing 401147, China

Correspondence to: Min Xie (minxie@nju.edu.cn) , Wei Zhao (zhaowei@nies.org)

Abstract: Observations of vertical wind profile in Chongqing, a typical mountainous city in China, are important, but sparse and have low resolution. To obtain more wind profile data, this study matched the Aeolus track with ground-based wind observation sites in Chongqing in 2021. Based on the obtained results, verification and quality control studies were conducted on the wind observations of a wind profile radar (WPR) with radiosonde (RS) data, and a comparison of the Aeolus Mie-cloudy and Rayleigh-clear wind products with WPR data was then performed. The conclusions can be summarized as follows: (1) A clear correlation between the wind observations of WPR and RS was found, with a correlation coefficient (R) of 69.92%. Their root-mean-square deviation increased with height, but decreased at height between 3 and 4 km. (2) After quality control of Gaussian filtering (GF) and empirical orthogonal function construction (EOFc, G = 87.23%) of the WPR data, the R between the WPR and RS reached 76.00% and 95.44%, respectively. The vertical distribution showed that GF could better retain the characteristics of WPR wind observations, but with limited improvement in decreasing deviations, whereas EOFc performed better in decreasing deviations, but considerably modified the original characteristics of the wind field, especially regarding intensive vertical wind shear in strong convective weather processes. (3) In terms of the differences between the Aeolus and WPR data, 56.0% and 67.8% deviations were observed within ±5 m/s for Rayleigh-clear and Mie-cloudy winds vs. WPR winds, respectively. Vertically, large mean differences of both Rayleigh-clean and Mie-cloudy winds versus WPR winds appeared below 1.5 km, which is attributed to the prevailing quiet and small winds within the boundary layer in Chongqing, in this case the movement of molecules and aerosols is mostly affected by irregular turbulence. Additionally, large mean differences at the height range between 4 to 8 km for

37 Mie-cloudy versus WPR winds may be related to the high content of cloud liquid water in the middle

38 troposphere of Chongqing. (4) The differences in both Rayleigh-clear and Mie-cloudy versus WPR winds

39 had changed. Deviations of 58.9% and 59.6% were concentrated between ±5m/s for Rayleigh-clear

40 versus WPR winds with GF and EOFc quality control, respectively. In contrast, 69.1% and 70.2% of

41 deviations appeared between ±5 m/s for Rayleigh-clear versus WPR and EOFc WPR winds, respectively.

42 These results shed light on the comprehensive applications of multi-source wind profile data in

43 mountainous cities or areas with sparse ground-based wind observations.

44 **Keywords:** Wind profile radar, Aeolus satellite, data verification, data quality control, mountainous
45 city

46 **1 Introduction**

47 The detection of the atmospheric wind profile is essential for studying atmospheric dynamics,

48 interactions between weather and pollution, and predict extreme weather (Baker et al., 1995; King et al.,

49 2017; Stettner et al., 2019; Sun et al., 2022). Furthermore, the value of atmospheric wind observations

50 has been illustrated by assimilation applications in numerical weather prediction (Benjamin et al., 2004;

51 Weissmann and Cardinali, 2007; Michelson and Bao, 2008). In particular, wind fields within the

52 boundary layer are mostly turbulent and difficult to simulate using models without the assimilation of

53 wind observations (Belmonte and Stoffelen 2019; Simonin et al., 2014). For areas with complex terrain,

54 such as mountainous cities, individual ground-based observation stations usually have poor

55 representation, and thus vertical observations are essential (Sekuła et al., 2021; Lu et al., 2022b).

56 Therefore, unconventional wind profile observations are urgently required for analysis and assimilation

57 into numerical prediction models to describe the transport of mesoscale weather systems, as well as to

58 advance our knowledge of atmospheric component movement in the actual atmosphere.

59 Wind profile radar (WPR) data may partially compensate for the limitations of conventional wind

60 field observations. WPR detects the scattering effect of atmospheric turbulence on electromagnetic waves

61 to detect the Doppler effect signals of air movement, and is capable of providing horizontal wind vectors

62 with high temporal and vertical resolution (Weber et al., 1990; Dibbern et al., 2001). The automated,

63 continuous, and real-time vertical wind profiles from the WPR could fill the gaps in upper-air

64 observations, both in time continuity and vertical resolution. Terrain and climate characteristics in unique

65 regions could have different impacts on WPR echoes, resulting in separate data observation errors.

Deleted: , influenced by the topography of the Tibetan Plateau…

Deleted: to study

Deleted: et al.

70 Therefore, data verification, and occasionally adequate quality control, are required before the

71 application of WPR data in a specific region (Zhang et al., 2015; Guo et al., 2020). In comparison,

72 radiosonde (RS) data are often considered reliable atmospheric wind observations to verify WPR data

73 (Weber et al., 1990; Chen et al., 2021).

74   Owing to advances in satellite detection, wind fields acquired from satellites can supplement

75 conventional ground-based observations in space coverage. Atmospheric motion vector detection can

76 only extract the wind information of layers with clouds. The United States and Europe have successively

77 detected sea surface wind fields using microwave radiometers and scatterometers (Endlich et al., 1971;

78 Njoku et al., 1980; Gaiser et al., 2004; Barre et al., 2008). The World Meteorological Organization

79 regards the detection of global three-dimensional wind fields as one of the most challenging and

80 important meteorological observation missions in the 21st century (WMO, 2001). The United States and

81 Europe have conducted space-borne wind lidar measurement programs, as these are the best methods for

82 detecting three-dimensional wind fields (Beranek et al., 1989; Baker et al., 2008; Wernham et al., 2016).

83 The Aeolus satellite was launched following the European Space Agency's (ESA) fifth Earth Explorer

84 mission on August 22, 2018. As the world's first Doppler wind lidar in space, Aeolus has enabled the

85 continuous detection of global wind profiles from the ground to the lower stratosphere with a vertical

86 resolution of 0.25–1 km (Marseille et al., 2008; Reitebuch et al., 2006; Zhang et al., 2019). Therefore,

87 the wind profile data detected by Aeolus can compensate for the lack of spatial coverage and vertical

88 resolution of ground-based wind field observations to some extent.

89   Located at the edge of the Sichuan Basin, Chongqing is a typical mountainous city in China known

90 for its complex topography. Owing to the unique terrain, the mechanism of extreme weather, and

91 movement of atmospheric components in the city are intricate and complex, making vertical observations

92 essential. Interference sources for the vertical detection of WPR might form in mountainous areas, which

93 are different from those in plain areas. Thus, reasonable data verification and quality control should be

94 conducted before application to ensure the accuracy and representativeness of the WPR. The spatial

95 distribution of ground-based vertical wind observations in Chongqing is sparse, and it is worthwhile to

96 verify the performance of Aeolus wind products and apply them to related mechanistic studies or

97 numerical assimilation systems. To this end, wind profile observations of RS, WPR, and Aeolus were

98 collected and matched in terms of time and space for 2021 in Chongqing. Based on the matched results,

99 data verification and quality control of WPR wind observations were implemented using RS data, and

3

Deleted: 7

Deleted: and Stoffelen,

Deleted: 3

Deleted: and three-dimensional spatial structure

Deleted: forecasts

Deleted: determining the

Deleted: complicated

the performance of Aeolus wind products in Chongqing was analyzed to provide a scientific basis for multi-source wind profile data applications in mountainous cities. The remainder of this paper is organized as follows: the RS, WPR, and Aeolus data used in this study, the matching procedure, data verification, and quality control methods are described in Section 2; Section 3 presents the comparison and quality control results of the WPR and Aeolus wind profile data; finally, the main conclusions are summarized in Section 4.

2 Data and methods

2.1 Data

2.1.1 Ground-based wind profile data

Shapingba (57516; 106.27°E, 29.34°N) is a national weather station and the only RS station in Chongqing. Wind speed and direction at 0000 and 1200 UTC (universal time coordinated) were obtained from an L-band sounding system on vertical height levels every 1 s from the surface to 30 km in the air (Zhang et al., 2020). Shapingba station belonged to the network of the L-band sounding system by China Meteorological Administration. The operational radiosonde stations in China widely use GTS1 ditital radiosonde as key components of L-band sounding system, which have high accuracy within the troposphere in detecting fine resolution profiles of meteorological factors (Bian et al., 2011; Guo et al., 2016; Guo et al.,2021b).

There are two wind profile radars in Chongqing, one at Shapingba station and the other at Youyang station (57633; 108.76°E, 28.84°N). Radars can operate almost automatically and continuously, acquiring vertical profiles of horizontal wind speed and wind direction (Guo et al., 2021a). The WPR in Shapingba and Youyang are from the same manufacturer, sharing the same temporal and spatial vertical resolutions of 5 min and 120 m, and vertically detecting 48 and 45 layers up to 9360 and 8910 m, respectively.

RS wind data are generally reliable vertical observations. Considering Shapingba WPR is located at the same station with RS, while Youyang Station is 360 km away from the RS, therefore, the data verification of WPR wind observations was conducted based on Shapingba WPR and RS data in this study (Figure 1).

4

2.1.2 Aeolus wind products

Launched on August 22, 2018, the first space-borne Doppler wind lidar, Aeolus, developed by the ESA, has been circling in a sun-synchronous orbit at an altitude of approximately 320 km, with a 7-day repeat cycle (ESA, 2008). Based on the original detection information, a series of products was released by the ESA. The Aeolus Level-2B products can provide scientific wind products, which can be used to obtain wind profile data from the ground to approximately 30 km in the air, with a vertical resolution of 0.25–2 km and an uncertainty of 2–4 m/s, varying with height (Rennie, 2018; Chen et al., 2022). Level-2B wind products are classified into Rayleigh-clear and Mie-cloudy winds. Specifically, Rayleigh channels mainly detect wind fields with atmospheric molecules as tracers in the troposphere and lower stratosphere, whereas the Mie channel detects signals from aerosols and cloud droplet particles within the boundary layer or in the cloud (Witschas et al., 2020). In this study, the horizontal line-of-sight (HLOS) wind products of both Rayleigh and Mie channels were used. Additionally, the validity flag and
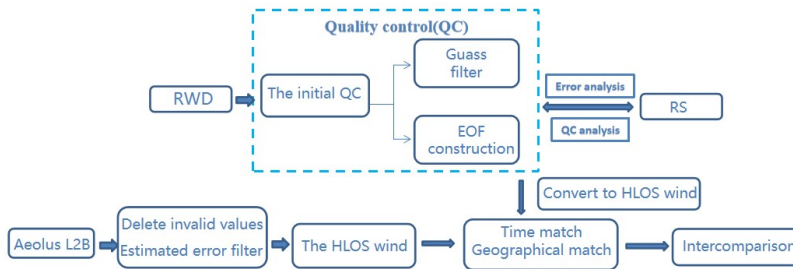
167 estimated errors were extracted for quality control of HLOS wind products (Tan et al., 2017; Guo et al.,

168 2021a).

2.2 Methods

2.2.1 Data matching and verification procedures

Figure 2: Flowchart of the multi-source wind profile data matching and verification procedures.

172 In an attempt to make full use of the multi-source vertical wind data from Chongqing, appropriate

173 procedures were used to match the RS, WPR, and Aeolus data in time and space considering the limited

174 ground-based wind profile observations. A flowchart of the procedure is shown in Figure 2.

175 First, data verification and quality control effect analysis of the Shapingba WPR were implemented

176 based on RS data. Based on the approach used by Zhang et al. (2016) and Guo et al. (2021a), the Aeolus

177 data were removed once the distances between adjacent tracks of Aeolus and ground-based sites

178 exceeded 1°. With this procedure, Shapingba station is not suitable for comparison with Aeolus data,

179 whereas Youyang WPR data is. Time and space matches of the WPR and Aeolus data were posed before

180 the comparison, the geographic location of WRP stations and Aeolus tracks are shown in Figure 1.

181 Specifically, because of the higher temporal resolution of WPR, the mean values of WPR data within 10

182 min before and after Aeolus sampling were used. Vertically, Aeolus data were interpolated and matched

183 to the layers of WPR data. Subsequently, Aeolus data were screened by validity flags and estimated

184 errors. Thereafter, both the original Youyang WPR detection and quality control data were converted

185 into HLOS winds for comparison with the Aeolus data. The WPR wind vector was projected onto the

186 HLOS winds using the following equation (Witschas et al., 2020):

$$v_{RWP_{HLOS}} = cos(\psi_{Aeolus} - wd_{RWP}) \cdot ws_{RWP} \qquad (1)$$

188 where ψ_{Aeolus} is the Aeolus azimuth angle, which could be extracted from the Level 2B products, while

189 wd_{RWP} and ws_{RWP} are WPR wind direction and speed, respectively.

192 **2.2.2 Statistical method**

193   The mean bias (MB) and root mean squared error (RMSE) were adopted as indicators (Equations 2

194 and 3) for the verification of the WPR and Aeolus wind products, which compares absolute and relative

195 deviations, respectively.

196
$$MB = \frac{1}{n}\sum_{i=1}^{n}\big(o(i) - r(i)\big) \qquad (2)$$

197
$$RMSE = \sqrt{\frac{\sum_{i=1}^{n}\big(o(i) - r(i)\big)^2}{n}} \qquad (3)$$

198 where $o(i)$ represents the observation values and $r(i)$ represents the referent values.

199 **2.2.3 Data quality control of the wind profile radar**

200 **2.2.3.1 The initial quality control**

201   The first step in quality control is to eliminate the abnormal increase of horizontal wind in a small

202 vertical range of WPR data, including screening invalid data exceeding the climate extreme values and

203 the vertical consistency test. The extreme climate wind values on the relative layers (Zuo 2020) are listed

204 in Table 1. For the vertical consistency test, if the wind difference between a specific layer and its

205 adjacent layer is greater than three times that of the two layers below, the value is considered as an

206 abnormal observation to be deleted (Zhang et al., 2015).

207 **Table 1: Extreme climate wind values in vertical layers**

Pressure(hPa)	1000	850	700	500	400	300	250
Height(m)	0	1500	3000	5500	7000	9000	10000
Extreme wind(m/s)	36.01	46.30	61.73	102.89	128.61	154.33	154.33

208 **2.2.3.2 Gaussian filtering (GF) method**

209   GF is a smooth filtering method that can be used to smooth out the details and noise of two-

210 dimensional graphs, and the observed value of the central point and its surrounding values are summed

211 in one-to-one correspondences. GF is similar to mean filtering, but its preset convolution operator

212 presents a Gaussian distribution. In this study, the convolutional operator was used to calculate the

213 weighted average of the WPR data to filter the high-frequency noise in the observation of WPR. The

214 Gaussian filtering function of the one-dimensional zero-mean normalization is as follows:

215
$$g(x) = \frac{1}{\sqrt{2\pi}\sigma} e^{\frac{x_2}{2\sigma^2}} \qquad (4)$$

where σ is the scale factor that determines the width of the Gaussian filter and further affects the degree of data smoothing. The larger the σ value, the wider the frequency band of the Gaussian filter, and the better the data smoothing effect. However, an excessively large σ value causes excessive data loss and distortion. In this study, σ was set to 3.

2.2.3.3 Empirical orthogonal function construction (EOFc) method

Based on the spatial-temporal sequence formed by wind field data W, calculations similar to empirical orthogonal decomposition were performed, and the main modes obtained by calculation were used to reconstruct the spatial-temporal sequence to construct new wind fields. Specifically, the X matrix is formed by selecting N times, a period of time before and after a certain moment, and L layers of effective data, vertically. X is represented below:

$$X = \begin{bmatrix} W_{1,1} & W_{1,2} & \cdots & W_{1,N} \\ W_{2,1} & W_{2,2} & & W_{2,1} \\ \vdots & \vdots & \ddots & \vdots \\ W_{L,1} & W_{L,2} & \cdots & W_{L,N} \end{bmatrix} \tag{5}$$

Subsequently, the covariance matrix of X, that is, S = XXT, and its eigenvalues and eigenvectors were calculated. According to the arrangement of the eigenvalues from largest to smallest, the cumulative interpretation variance of the first m eigenvectors can be expressed as follows:

$$G = \left(\sum_{k=1}^{m} \lambda_k\right) / \left(\sum_{k=1}^{L} \lambda_k\right) \tag{6}$$

The larger the eigenvalue corresponding to the eigenvector, the more its corresponding distribution reflects the typical characteristics of the original field. The time coefficient T = ETX was calculated with the eigenvector E. Finally, the main modes decomposed by EOF were used to reconstruct the time series within N times, following the use of X = ET to obtain the vertical distribution of the wind field at the corresponding time. In the reconstruction of the time series, a cut-off threshold (G $\geq$85%) was set for the interpretation of the cumulative variance to control the quality of the observed data.

Assuming that the cumulative interpretation variances of the first m feature vectors met G $\geq$85%, and the first m-1 did not meet G $\geq$85%, the feature vectors of the first m modes were adopted in the reconstruction of the sequence, and the corresponding winds at moment j of the ith altitude layer are:

$$WS_{i,j} = \sum_{k=1}^{m} e_{i,k} \, t_{k,j} \tag{7}$$

243   The EOFc method can eliminate outliers and pulsating noise from observation data, and has been

244   applied in quality control research of observational elements in previous studies, such as in Qin et al.

245   (2010).

246   **2.2.4 Quality control of Aeolus wind products**

247   The quality of the Aeolus HLOS wind products is controlled by validity flags and estimated errors,

248   which are also present in Level 2 B data products. Only data with flags equal to 1 were considered valid.

249   The data were subsequently filtered according to estimated errors, the theoretical values calculated based

250   on the measured signal levels, and the temperature and pressure sensitivity of the Rayleigh channel

251   response (Dabas et al., 2008). Previous studies have revealed that notable observation errors appeared

252   when the estimated errors were large (Witschas et al., 2020). Consequently, thresholds for estimated

253   errors of 7(5) m/s were applied for Rayleigh(Mie) winds in this study, based on the method described by

254   Guo et al. (2021a).

255 **3 Results and discussion**

256 **3.1 Data verification and quality control of WPR**
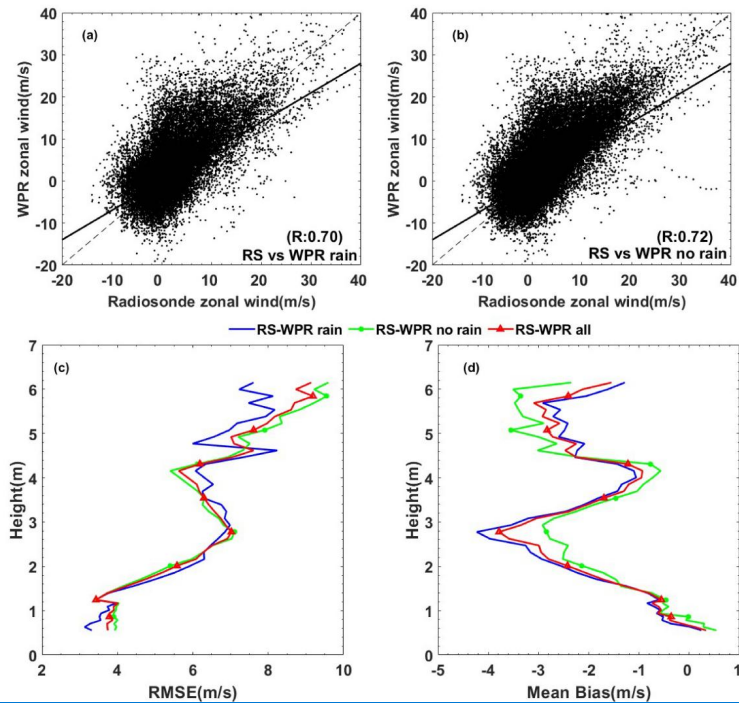
257

258 Figure 3. Scatter-plots for wind profile radar (WPR) vs radiosonde (RS) data during (a) rainy days and (b)
259 no rainy days, and vertical distribution of (c) root mean squared error (RMSE) and (d) mean bias (MB) for
260 WPR vs RS during all days, rainy days and no rainy days.

261 Data verification and quality control of the Shapingba WPR were performed based on RS data from

262 the same station. The WPR detects data vertically above the station, while the RS data are derived from

263 air balls, which can respectively drift as far as 0-90, 2-25 and <10km at 200, 500 and 850hPa away

264 from the releasing station (Zeng et al., 2019). Therefore, certain differences exist in the spatial sampling

265 of WPR and RS. Assuming that the atmospheric horizontal distribution is uniform within dozens of

266 kilometers, the WPR and RS wind fields will be comparable. Additionally, the exact release times of the

267 air balls were 23:15 and 11:15 UTC, and they generally took 25 min to rise to 10 km. Therefore, the

268 mean values of the 23:15–00:00 and 11:15–12:00 WPR data were processed to compare the WPR and

271 RS data. Finally, for comparison with the Aeolus data, wind fields derived from WPR and RS data were

272 converted into zonal wind components for data verification and quality control.

273   To clarify influences of weather, especially precipitation, on wind profile radar observation quality,

274 scatter plots and vertical distribution of statistical parameters for WPR versus RS during rainy days and

275 no rainy days were given in Figure 3. Between 1.5 and 4.5km, WPR deviations during rainy days exceed

276 a little that without rain, and the RMSE and MB between WPR and RS are slightly smaller during rainy

277 days than that without rain below 1.5km and above 4.5km. The correlation coefficient between WPR and

278 RS with rain is a bit lower than that without rain. Generally speaking, precipitation can affect WPR

279 observation quality, but the deviation distributions are overall the same during rainy and no rainy days,

280 with slight differences on different layers. As a result, we discussed the quality control effects of WPR

281 data based on all data, including rainy days and no rain days.
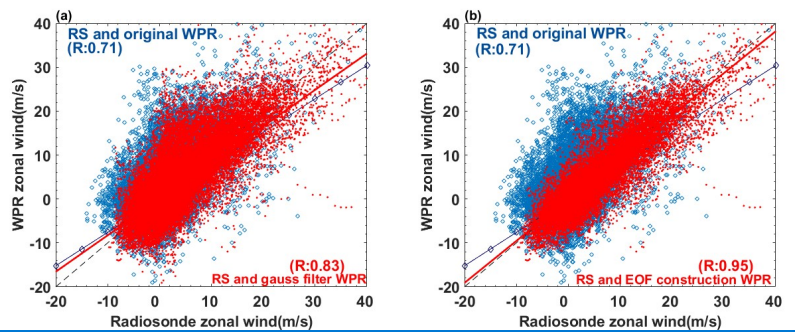
282

Figure 4: Scatter-plots for (a) original and Gaussian filtering (GF) WPR vs RS data, (b) original and empirical orthogonal function construction (EOFc) WPR vs RS data.

283

284   Based on quality control 1 of the WPR data mentioned above, 784 invalid wind speed data were

285 filtered, after which GF and EOFc were conducted on WRP winds. The blue dots in Figure 4 represent

286 the scattered distributions of the original WPR and RS data. The correlation coefficient(R) was 69.92%,

287 with scatters distributed along the reference line, indicating a correlation between the two types of data.

288 Large numbers of dots with significant deviation from the reference line between the wind speeds of $\pm$

289 10 m/s implied large differences between the WPR and RS in the observation of low wind speeds. The

290 red dots in Figure 4(a) are scatter plots of GF-controlled WPR and RS, with an R of 76.00%, showing

291 better correlation compared with the original WPR and RS wind data. The GF method screened parts of

292 the data far away from the reference line, which are wind data with large differences between WPR and

297 RS, contributing to an improvement in the correlation of the two types of data. The performance of the

298 WPR data quality control based on EOFc is more significant in Figure 4(b) compared to GF. For EOFc,

299 G was selected to be greater than 85% for the first time; specifically, the first two modes were added

300 after EOF decomposition, with G = 87.23%. The R between the EOFc WPR and RS winds reached

301 95.44%, with scatters more concentrated around the reference line compared with the original and GF

302 WPR.
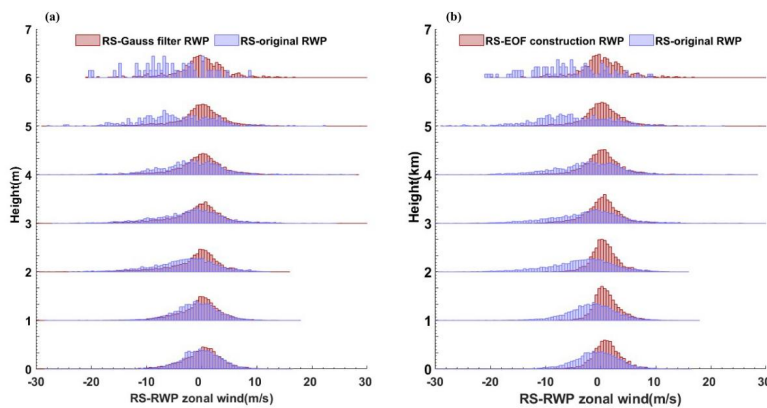
303

Figure 5: Probability density distributions vertical variations of (a) RS minus original and GF WPR data, (b) RS minus EOFc WPR data.

304

305   The vertical wind deviation distributions of the original and quality-controlled WPR are shown in

306 Figure 5, and the vertical distributions of the statistical parameters are shown in Figure 5. The distribution

307 of deviations between the RS and original WPR data followed normal distribution on various layers. The

308 median of the distribution was centred around 0 near ground within 2km, and gradually moved towards

309 to the negative values above 2km, indicating significant negative deviations on the upper layers. Large

310 negative deviations emerged on different layers, however, large positive deviations were mainly

311 distributed around 3-5 km, with the maximum around 30 m/s. From the perspective of statistical

312 parameters, the RMSE of RS and the original WPR deviation increased with height overall, but decreased

313 at heights between 3 and 4 km. The vertical MB distribution between the RS and original WPR data

314 presented an M-shaped distribution, with positive MB values near the ground and negative values in the

315 other layers. According to the vertical distribution of the deviation scatter points, the negative deviations

316 are significantly larger than the positive deviations. For a relatively small MB value of approximately 4

323 km, some of the large positive deviations in Figure 5 at this level balance the negative values. Similarly,

324 large positive and negative deviations appeared at approximately 6 km, forming small MB values at this

325 level. In general, wind speeds increase with height, leading to an increase in the observation deviations

326 of the WPR.
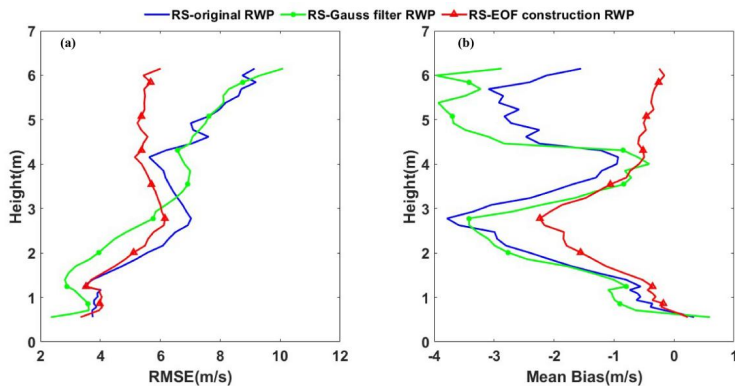
327

Figure 6: Vertical distributions of RMSE and MB for (a) RS vs GF WPR data, (b) RS vs EOFc WPR data.

328

329   Taking RS data as true values, the zonal WPR wind data in Chongqing exhibited various detection

330 errors with height, indicating that quality control of the original WPR data is necessary. The red

331 histograms in Figure 5(a) represent the vertical deviation distributions between RS data and the GF WPR

332 with respect to height. Compared with the original WPR data, GF eliminates some large deviation values

333 of different layers, making the distribution more centred around 0, especially on the upper layers. The

334 vertical distributions of the RMSE and MB between the RS and WPR data corresponded to modifications.

335 The RMSE of the RS and GF WPR data is reduced below 3 km compared to the original WPR, while

336 the alteration of MB mainly manifests above 4 km. Remarkably, the negative value of MB above 4 km

337 increased after GF in the WPR data. This was because of the reduction in the larger positive deviation

338 value, and the negative deviation could not be offset. Subsequently, the EOFc method was adopted for

339 the zonal winds in the original WPR data. The vertical deviation distributions of RS and EOFc WPR

340 reduced many large negative deviations in the different vertical layers, making distribution more in line

341 with normal distribution(Figure 5b). The statistical parameters of the vertical distribution also showed

342 significant changes compared to the original data. A significant decrease in the RMSE value and a notable

Deleted: 3

Formatted: Justified

Deleted: **4**

Deleted: **the root mean squared error (**

Deleted: **)**

Deleted: **mean bias (**

Deleted: **)**

Deleted: **Radiosonde (**

Deleted: **)**

Deleted: **original and Gaussian filtering (**

Deleted: **)**

Deleted: **wind profile radar (**

Deleted: **)**

Deleted: **empirical orthogonal function construction (**

Deleted: **)**

Deleted: 3

Deleted: 3

346 reduction in the negative MB above 1 km were observed between the RS and EOFc WPR (Figure 6).

347 Combining both the vertical distribution for deviation scatters and statistical parameters, the EOFc WPR

348 winds were similar to the RS data at various heights. Although the deviations of the two types of data

349 were significantly reduced, it is worth noting that the EOFc WPR data have modified the characteristics

350 of the original wind fields to a large extent, especially under strong convective weather conditions with

351 large vertical wind shear. In comparison, the GF WPR data could better retain the basic characteristics

352 of the original wind fields. However, the GF method exhibited a limited reduction in the detection

353 deviations of the WPR data. In general, the two quality control methods have different effects on the

354 reduction of detection deviations and the retention of the original information.

355 **3.2 Comparison of the Aeolus and WPR wind data**
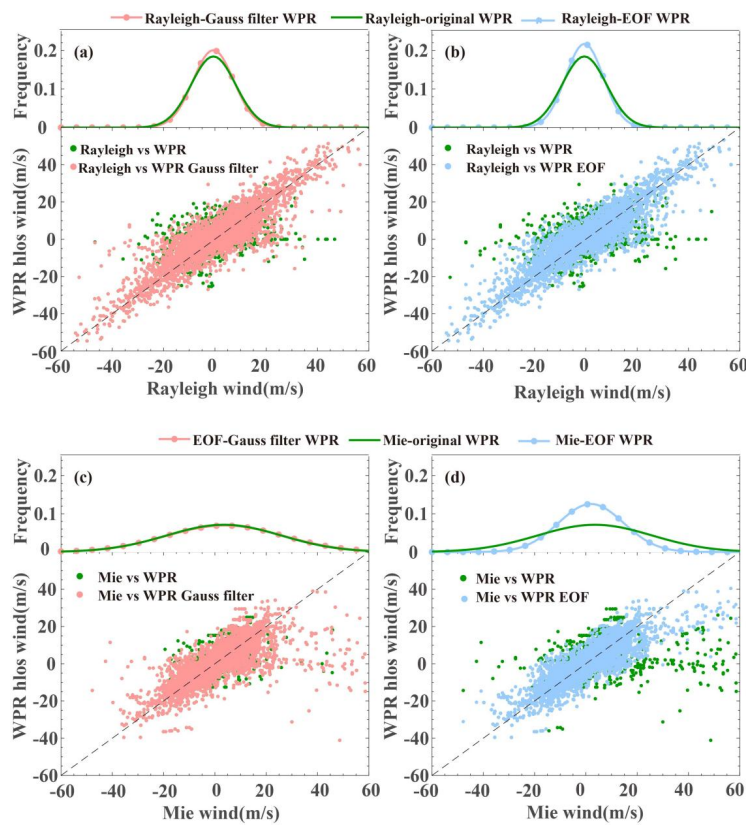
356

Figure 7: Probability density distributions of deviations and scatter-plots between (a) Rayleigh-clear and (c) Mie-cloudy vs WPR original and GF WPR winds, (b) Rayleigh-clear and (d) Mie-cloudy vs original and EOFc WPR winds.

Owing to the limited spatial coverage of ground-based wind profile data, data verification of Aeolus products in Chongqing was conducted to compensate for the spatial coverage of wind observations to some extent. The obtained results indicate that the Youyang WPR data can be used to verify the Aeolus products described in Section 2. The probability density distribution (PDD) and scatter plots of both Aeolus Rayleigh-clear and Mie-cloudy products versus WPR data are shown in Figure 7. The PDD of deviations between Rayleigh-clear and WPR in Figure 7(a) generally present as a Gaussian distribution, with 82.9% of deviations concentrated between ± 10 m/s and 56.0% of deviations between ± 5 m/s. Quality control with the GF and EOFc methods was conducted on original WPR observations, and the PDD of deviations between Rayleigh-clear and quality-controlled WPR winds were concentrated around 0. For deviations between Rayleigh-clear and GF WPR winds, 85.8% of deviations were centralized between ± 10 m/s and 58.9% of deviations between ± 5 m/s. In comparison, 86.3% of deviations of Rayleigh-clear and EOFc WPR winds appeared between ± 10 m/s and 59.6% of deviations between ± 5 m/s. The scatter distributions of the Rayleigh-clear and WPR winds were shown in Figure 7(a) and 7(b), respectively. A good correlation between Rayleigh-clear and original WPR data was observed, except for some dots far from the reference line, which were scattered with large deviations between the Aeolus and WPR data. Better correlations were observed between the Rayleigh-clear and quality-controlled WPR winds with more scatter centralized around the reference line. Figure 7(c)–(d) show the PDD distribution and scatter plots of the deviations between the Mie-cloudy and WPR winds. 86.2% of deviations of Mie-cloudy versus original WPR data were centralized between ±10 m/s and 67.8% of deviations between ±5 m/s, while 86.9% of deviations of Mie-cloudy versus GF WPR winds were centralized between ±10 m/s and 69.1% of deviations between ±5 m/s. For the EOFc WPR winds, 87.5% of deviations appeared between ±10 m/s and 70.2% of deviations between ±5 m/s. First, the deviations of the Mie-cloudy and quality-controlled WPR data were more concentrated around 0 compared with the original RWP. Most of the scatter points between the Mie-cloudy and original RWP winds were centralized near the reference line. However, a number of dots were concentrated around ± 20 m/s for the WPR winds, and much larger values for the Aeolus data appeared away from the reference line.

Deleted: **5**
Deleted: **Gaussian filtering (**
Deleted: **)**
Deleted: **empirical orthogonal function construction (**
Deleted: **)**
Deleted: 5
Deleted: 5
Deleted: are
Deleted: 5
Deleted: 5
Deleted: 5
Deleted: We found that

392 Additionally, compared with Rayleigh-clear winds, deviations in the Mie-cloudy versus WPR data were
393 small, which may be attributed to the detection principles of the two channels. Compared with the
394 Rayleigh channel, the tracers for the Mie channel, including aerosols and cloud droplets within the
395 boundary layer and in the cloud, mainly centralized at lower vertical levels with smaller wind speeds,
396 resulting in smaller wind deviations for the Mie-cloudy observations.
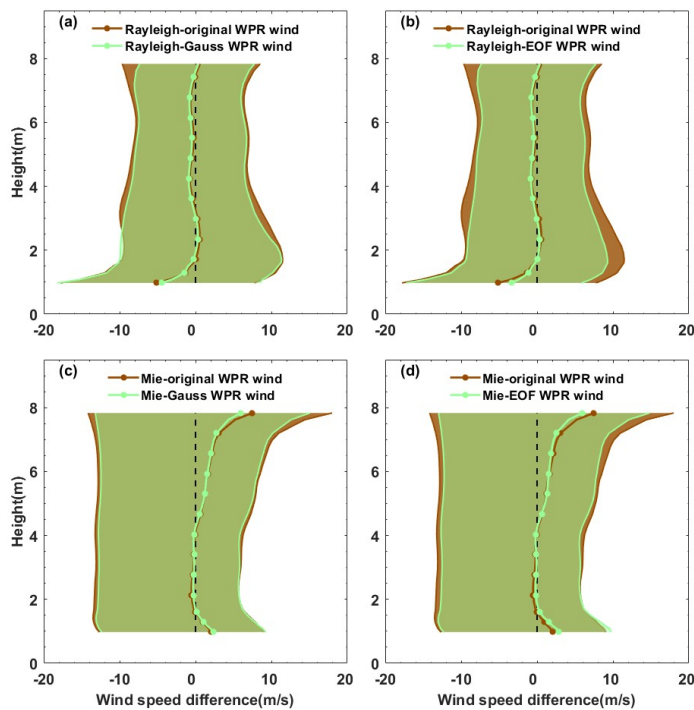
397

Figure 8: Vertical distribution of mean differences and deviations between (a) Rayleigh-clear vs GF WPR data, (b) Rayleigh-clear vs original and EOFc WPR data, (c) Mie-cloudy vs original and GF WPR data and (d) Mie-cloudy vs original and EOFc WPR data.

398

399 Figure 8 shows the vertical distribution characteristics of the differences between Aeolus products
400 and RWP data. The red solid line represents the vertical distributions of the mean differences between
401 Aeolus and the original RWP data, and the shaded areas denote positive and negative deviations from
402 the mean differences. Mean differences between the Rayleigh-clear and original WPR winds have large
403 negative deviations below 1.5 km, with the maximum deviation reaching -5.2-13.0, -5.2+12.61 m/s.

Deleted: **6**

Deleted: **original and Gaussian filtering (**

Deleted: **)**

Deleted: **wind profile radar (**

Deleted: **)**

Deleted: **empirical orthogonal function construction (**

Deleted: **)**

Deleted: 6

405 However, the mean difference between these data maintained within ± 1 m/s from the heights of 1.5 to

406 8km, with simultaneous decreasing negative and positive deviations with height. The wind measurement

407 capability of the Rayleigh channel is largely limited by the receiving intensity, and the Sichuan Basin is

408 one of the large-value aerosol regions in China (Zhang et al., 2012; Lu et al., 2022a). Particularly, below

409 1.5 km within the boundary layer, strong aerosol scattering will inevitably affect molecular scattered

410 signals, thus reducing the accuracy of Rayleigh channel wind field inversion (Tan et al., 2017; Guo et al.,

411 2021a). In contrast, the vertical distribution of mean differences between Mie-cloudy and original RWP

412 data (Figure 8c and d) showed large values within the boundary layer (below 1.5 km) and middle

413 troposphere (4–8 km). The maximal deviation within the boundary layer reached 2.09-18.23, 2.09+14.76

414 m/s, while the maximal values were 7.49-19.98, 7.49+21.64 m/s in the middle troposphere. For the Mie

415 channel, aerosols and cloud droplet particles were used as tracers for wind measurements. Owing to the

416 influence of the topography in Chongqing, the prevailing quiet and small winds within the boundary

417 layer result in the dominant influence of turbulent motion on large particles (Lu et al., 2022b). This

418 contributes to larger deviations in Mie wind observations because of the irregularity of turbulence. The

419 notable mean differences in the middle troposphere may be affected by the distribution of cloud droplets.

420 Previous studies have revealed that due to the influence of the topography of the Tibetan Plateau, the

421 liquid cloud water contents around 27°N to 35°N in central China are remarkably larger than those in the

422 southern and northern regions at the same altitude (Yang et al., 2012), with nimbostratus and altostratus

423 prevailing in the affected areas (Yu et al., 2004). These may contribute to large mean differences and

424 deviations between Mie winds and WPR data at altitudes of 4–8 km in Chongqing, which is located on

425 the eastern side of the Tibetan Plateau. According to existing observations, the frequency of cloud

426 occurrence in the middle troposphere in spring, autumn, and winter is higher than that in summer, which

427 can explain to some extent why the annual mean differences between Mie winds and RWP around 4–8

428 km have large values, whereas the average values in summer do not (Guo et al., 2021a). Based on the

429 GF and EOFc quality control of the WPR data, the mean differences between the Rayleigh-clear and

430 WPR winds were found to not change significantly, with only some reduction in the differences between

431 the Rayleigh-clear and EOFc WPR data within the boundary layer. However, by controlling the WPR

432 data quality, the positive and negative deviations of the mean difference at various heights can be

433 effectively reduced (Figure 8a and 6b). Specifically, GF can reduce deviations above 3 km, whereas

434 EOFc modifies the positive deviations within the boundary layer. For the Mie winds, a remarkable

1

Deleted: at a height of 1 km,

Deleted: was

Deleted: 6

Deleted: 6

439 reduction was observed for mean differences at an altitude of approximately 6–8 km and deviations in

440 various layers with quality-controlled WPR data compared with the original WPR data.

4 Conclusions

442 To evaluate the observation quality of the multi-source wind profile data in Chongqing, this study

443 matched the Aeolus, RS, and WPR data for 2021. The matching results indicate that the Youyang WPR

444 can be used for comparison with the Aeolus winds. Additionally, data verification and quality control

445 studies of ground-based WPR data were conducted based on Shapingba RS wind observations. The main

446 conclusions are as follows:

447 A correlation was found between the RS and original WPR zonal wind data, with an R of 69.92%

448 and scatter points generally distributed along the reference line. The RMSEs of the RS and WPR data

449 increased with height overall, except at an increase of approximately 3–4 km. The MB wasis vertically

450 distributed in an M-shape, with relatively smaller MB values appearing at 4 and 6 km because of the

451 cancellation of positive and negative deviations.

452 Following screened by the extreme wind climate values and the vertical consistency test, 784 WPR

453 wind observations were eliminated. The R between RS versus GF WPR data and EOFc (G = 87.23) WPR

454 data were 76.00% and 95.44%, respectively, demonstrating a better correlation between RS and EOFc

455 WPR data. A comparison of the deviations in the vertical distribution of the RS and WPR data before

456 and after quality control revealed that the EOFc WPR data are closer to RS winds at various heights,

457 resulting in smaller deviations between the two. However, it should be noted that the EOFc WPR winds

458 have a broader filter than the original data, which can remarkably alter the characteristics of the original

459 wind fields, particularly in cases of severe convection weather conditions where there are significant

460 vertical wind shears. While preserving the basic features of the original wind field, the GF method has a

461 limited impact on reducing the deviations of the original WPR wind observations.

462 The Rayleigh and Mie winds detected by Aeolus exhibited various deviations from the WPR data;

463 56.0% of deviations between Rayleigh-clear and WPR data existed within ± 5 m/s, while 67.8% of

464 deviations existed between Mie-cloudy and 67.8% of deviations between WPR data were_ within ± 5

465 m/s. The Mie channel detects aerosols and cloud droplets as tracers, which are lower than the height

466 layers detected by the Rayleigh channel, resulting in relatively small wind speed deviations. However,

467   the mean differences between Rayleigh-clear and WPR winds are smaller than those of Mie-cloudy winds,

468   especially in the middle troposphere of 4–8 km. This may be due to the influence of the topography of

469   the Tibetan Plateau, resulting in a remarkable increase in the liquid cloud water content from 27°N to

470   35°N in central China compared to other regions. Chongqing is located in the affected areas; thus, the

471   accuracy of Mie wind observations is influenced by the middle troposphere.

472   The deviations between the Aeolus and WPR data changed to some extent after quality control of

473   the WPR data, both for the Rayleigh-clear and Mie-cloudy winds. The scatter points of the Aeolus and

474   WPR data, which were far away from the reference line, decreased; 58.9% of deviations between the

475   Rayleigh-clear and GF WPR data were centralized between ± 5 m/s, and 59.6% of deviations for EOFc

476   WPR data were within ± 5 m/s. For the Mie channel, 69.1% of deviations were concentrated ± 5 m/s

477   between the satellite and GF WPR data, and 70.2% of deviations existed between the Mie and EOFc

478   WPR data. The mean differences of the Rayleigh channel and WPR data changed little after quality

479   control was conducted using both the GF and EOFc methods on WPR data; however, both positive and

480   negative deviations to the mean values decreased. For Mie winds, quality control on WPR made distinct

481   modifications to the mean differences between 6–8 km and deviations to the mean values of all layers

482   between Mie-cloudy and WPR data.

491   **Conflicts of Interest:** The authors declare no conflict of interest.

492   **Reference**

493   Baker W. 2008. Doppler wind lidar: current activities and future plans//Winter T-PARC Workshop.
494   [s.l.]: NOAA/NASA/DoD Joint Center for Satellite Data Assimilation.

495   Baker, W. E., Emmitt, G. D., Robertson, F. R., Atlas, R., Molinari, J. E., Bowdle, D. A., Paegle, J. N.,
496   Hardesty, R. M., Menzies, R. T., Krishnamurti, T. N., Brown, R. A., Post, M. J., Anderson, J.
497   R., Lorenc, A. C., and McElroy, J. L. 1995. Lidar-measured winds from space: A key

498   component for weather and climate prediction, Bulletin of the American Meteorological
499   Society 76, 869-888.

500   Barre H M J P, Duesmann B and Kerr Y H. 2008. SMOS: the mission and the system. IEEE
501   Transactions on Geoscience and Remote Sensing, 46(3): 587-593.

502   Belmonte Rivas, M., and Stoffelen, A. 2019. Characterizing ERA-Interim and ERA5 surface wind
503   biases using ASCAT, Ocean Sci. 15, 831-852.

504   Benjamin, S. G., Schwartz, B. E., Szoke, E. J., and Koch, S. E. 2004. The Value of Wind Profiler Data
505   in U.S. Weather Forecasting, Bulletin of the American Meteorological Society 85, 1871-1886.

506   Beranek R G, Bilbro J W, Fitzjarrald D E, Jones W D, Keller V W and Perrine B S. 1989. Laser
507   atmospheric wind sounder (LAWS)//Proceedings of SPIE 1062, Laser Applications in
508   Meteorology and Earth and Atmospheric Remote Sensing. Los Angeles: SPIE: 234-248.

509   Bian, J., Chen, H., Vömel, H. et al. Intercomparison of humidity and temperature sensors: GTS1,
510   Vaisala RS80, and CFH. Adv. Atmos. Sci. 28, 139–146. 2011. https://doi.org/10.1007/s00376-
511   010-9170-8

512   Chen, C., Xue, X., Sun, D., Zhao, R., Han, Y., Chen, T., et al. 2022. Comparison of lower stratosphere
513   wind observations from the USTC's Rayleigh Doppler lidar and the ESA's satellite mission
514   Aeolus. Earth and Space Science, 9, e2021EA002176.

515   Chen, Z.-Y., Chu, Y.-H., and Su, C.-L. 2021. Intercomparisons of Tropospheric Wind Velocities
516   Measured by Multi-Frequency Wind Profilers and Rawinsonde, Atmosphere 12, 1284.

517   Dabas, A., Denneulin, M. L., Flamant, P., Loth, C., Garnier, A., and Dolfifi-Bouteyre, A.: Correcting
518   winds measured with a Rayleigh Doppler lidar from pressure and temperature effects, Tellus
519   A, 60, 206–21.

520   Endlich R M, Wolf D E, Hall D J and Brain A E. 1971. Use of a pattern recognition technique for
521   determining cloud motions from sequences of satellite photographs. Journal of Applied
522   Meteorology, 10(1): 105-117.

523   European Space Agency (ESA): "ADM-Aeolus Science Report," 2008. ESA SP-1311, 121 p.,
524   http://esamultimedia.esa.int/docs/SP-1311_ADM-Aeolus_FINAL_low-res.pdf,

525   Gaiser P W, St Germain K M, Twarog E M, Poe G A, Purdy W, Richardson D, Grossman W, Jones W
526   L, Spencer D, Golba G, Cleveland J, Choy L, Bevilacqua R M and Chang P S. 2004. The
527   WindSat spaceborne polarimetric microwave radiometer: sensor description and early orbit
528   performance. IEEE Transactions on Geoscience and Remote Sensing, 42(11): 2347-2361.

529   Guo, J., Liu, B., Gong, W., Shi, L., Zhang, Y., Ma, Y., Zhang, J., Chen, T., Bai, K., Stoffelen, A., de
530   Leeuw, G., and Xu, X. 2021. Technical note: First comparison of wind observations from

531   ESA's satellite mission Aeolus and ground-based radar wind profiler network of China,
532   Atmos. Chem. Phys. 21, 2945-2958.

533 Guo, J., Miao, Y., Zhang, Y., Liu, H., Li, Z., Zhang, W., He, J., Lou, M., Yan, Y., Bian, L., and Zhai,
534   P. 2016. The climatology of planetary boundary layer height in China derived from
535   radiosonde and reanalysis data, Atmos. Chem. Phys., 16, 13309–13319,
536   https://doi.org/10.5194/acp-16-13309-2016.

537 Guo, J., Zhang, J., Yang, K., Liao, H., Zhang, S., Huang, K., Lv, Y., Shao, J., Yu, T., Tong, B., Li, J.,
538   Su, T., Yim, S. H. L., Stoffelen, A., Zhai, P., and Xu, X. 2021. Investigation of near-global
539   daytime boundary layer height using high-resolution radiosondes: first results and comparison
540   with ERA5, MERRA-2, JRA-55, and NCEP-2 reanalyses, Atmos. Chem. Phys., 21, 17079–
541   17097, https://doi.org/10.5194/acp-21-17079-2021.

542 King, G. P., Portabella, M., Lin, W., and Stoffelen, A. 2017.Correlating extremes in wind and stress
543   divergence with extremes in rain over the Tropical Atlantic, EUMETSAT Ocean and Sea Ice
544   SAF Scientifific Report OSI_AVS_15_02, Version 1.0, available at: http://www.osi-
545   saf.org/?q$=$_content/correlating-extremeswind-and-stress-divergence-extremes-rain-over-
546   tropical-atlantic).

547 Lu, H., Xie, M., Liu, B., Liu, X., Feng, J., Yang, F., Zhao, X., You, T., Wu, Z., and Gao, Y. 2022a.
548   Impact of atmospheric thermodynamic structures and aerosol radiation feedback on winter
549   regional persistent heavy particulate pollution in the Sichuan-Chongqing region, China,
550   Science of The Total Environment 842, 156575.

551 Lu, H., Xie, M., Liu, X., Liu, B., Liu, C., Zhao, X., Du, Q., Wu, Z., Gao, Y., and Xu, L. 2022b. Spatial-
552   temporal characteristics of particulate matters and different formation mechanisms of four
553   typical haze cases in a mountain city, Atmospheric Environment 269, 118868.

554 Marseille G J, Stoffelen A and Barkmeijer J. 2008. Impact assessment of prospective spaceborne
555   Doppler wind lidar observation scenarios. Tellus A: Dynamic Meteorology and
556   Oceanography, 60(2): 234-248.

557 Michelson, S., and Bao, J.-W. 2008. Sensitivity of Low-Level Winds Simulated by the WRF Model in
558   California's Central Valley to Uncertainties in the Large-Scale Forcing and Soil Initialization,
559   Journal of Applied Meteorology and Climatology - J APPL METEOROL CLIMATOL 47,
560   3131-3149.

561 Njoku E, Christensen E and Cofield R. 1980. The Seasat scanning multichannel microwave radiometer
562   (SMMR): antenna pattern corrections-Development and implementation. IEEE Journal of
563   Oceanic Engineering, 5(2): 125-137.

564 Reitebuch O, Paffrath U and Leike I. 2006. ATBD: ADM-Aeolus Level 1B Product. European Space
565   Research and Technology Centre.

566   Rennie, M. P. 2018. An assessment of the expected quality of Aeolus Level-2B wind products, EPJ
567   Web Conf., 176, 02015, https://doi.org/10.1051/epjconf/201817602015,

568   Sekuła, P., Bokwa, A., Bartyzel, J., Bochenek, B., Chmura, Ł., Gałkowski, M., and Zimnoch, M. 2021.
569   Measurement report: Effect of wind shear on PM10 concentration vertical structure in the
570   urban boundary layer in a complex terrain, Atmospheric Chemistry & Physics 21, 12113-
571   12139.

572   Simonin, D., Ballard, S., and Li, Z. 2014. Doppler radar radial wind assimilation using an hourly
573   cycling 3D-Var with an 1.5km resolution version of the Met Office Unified Model for
574   Nowcasting, Quarterly Journal of the Royal Meteorological Society 140.

575   Stettner, D., Velden, C., Rabin, R., Wanzong, S., Daniels, J., and Bresky, W. 2019. Development of
576   enhanced vortex-scale atmospheric motion vectors for hurricane applications, Remote Sens.,
577   11, 1981, https://doi.org/10.3390/rs11171981.

578   Sun, X., Zhou, Y., Zhao, T., Bai, Y., Huo, T., Leng, L., He, H., and Sun, J. 2022. Effect of Vertical
579   Wind Shear on PM2.5 Changes over a Receptor Region in Central China, Remote Sensing 14,
580   3333.

581   Tan, D., Rennie, M., Andersson, E., Poli, P., Dabas, A., de Kloe, J., Marseille, G.-J., and Stoffelen, A.
582   2017. Aeolus Level-2B Algorithm Theoretical Basis Document, Tech. rep., AE-TN-
583   ECMWFL2BP- 0023, v. 3.0, 109 pp.

584   Weber, B. L., & Wuertz, D. B. 1990. Comparison of Rawinsonde and Wind Profiler Radar
585   Measurements, Journal of Atmospheric and Oceanic Technology, 7(1), 157-174.

586   Weissmann, M., and Cardinali, C. 2007. Impact of airborne Doppler lidar observations on ECMWF
587   forecasts, Quarterly Journal of the Royal Meteorological Society 133, 107-116.

588   Wernham D, Ciapponi A, Riede W, Allenspacher P, Era F, D'Ottavi A and Thibault
589   D. 2016. Verification for robustness to laser-induced damage for the Aladin instrument on the
590   ADM-Aeolus satellite//Proceedings of SPIE 10014, Laser-Induced Damage in Optical
591   Materials 2016. Boulder: SPIE: 1001408.

592   Witschas, B., Lemmerz, C., Geiß, A., Lux, O., Marksteiner, U., Rahm, S., Reitebuch, O., and Weiler,
593   F. 2020. First validation of Aeolus wind observations by airborne Doppler wind lidar
594   measurements, Atmos. Meas. Tech. 13, 2381-2396.

595   Yang Dasheng, Wang Pucai. 2012. Characteristics of Vertical Distributions of Cloud Water Contents
596   over China during Summer[J]. Chinese Journal of Atmospheric Sciences, 36(1): 89-101.

597   Yu, R., Wang, B., & Zhou, T. 2004. Climate Effects of the Deep Continental Stratus Clouds Generated
598   by the Tibetan Plateau, Journal of Climate, 17(13), 2702-2713.

Deleted:

Zeng, Z., Mao, F., Wang, Z., Guo, J., Gui, K., An, J., et al . 2019. Preliminary evaluation of the
atmospheric infrared sounder water vapor over China against high-resolution radiosonde
measurements. Journal of Geophysical Research: Atmospheres, 124, 3871－3888.
https://doi.org/10.1029/2018JD029109

Zhang C L, Sun X J, Zhang R W, Zhao S J, Lu W, Liu Y W and Fan Z Q. 2019. Impact of solar
background radiation on the accuracy of wind observations of spaceborne Doppler wind lidars
based on their orbits and optical parameters. Optics Express, 27(12): A936-A952.

Zhang, W., Guo, J., Miao, Y., Liu, H., Zhang, Y., Li, Z., and Zhai, P. 2016. Planetary boundary layer
height from CALIOP compared to radiosonde over China, Atmos. Chem. Phys. 16, 9951-
9963.

Zhang Xubin, Wan Qilin, Xue Jishan, Ding Weiyu, Li Haorui. 2015. Quality control of wind profile
radar data and its application to assimilation[J]. Acta Meteorologica Sinica, (1): 159-176.

Zhang, X., Wang, Y., and Niu, T. 2012. Atmospheric aerosol compositions in China: Spatial/temporal
variability, chemical signature, regionalhaze distribution and comparisons with global
aerosols, Atmos Chem Phys 58, 26571-26615.

Zhang, Y., J. Guo, Y. Yang, Y. Wang, and S.H.L. Yim. 2020. Vertical wind shear modulates
particulate matter pollutions: A perspective from Radar wind profiler observations in Beijing,
China. Remote Sensing, 12(3), 546.

Zuo Q. M.S. 2020. Research on Quality Control Methods and Assimilation Application of Wind
Profiler Radar Data. Nanjing: Nanjing University of Information Science and Technology.